

Numerical Conductivity Reconstruction from Partial Interior Current Density Information in Three Dimensions

Hassan Yazdanian ^{1,*} and Kim Knudsen ²

¹ Department of Biomedical Engineering, K. N. Toosi University of Technology, Tehran, Iran

² DTU Compute, Technical University of Denmark, 2800 Kgs. Lyngby, Denmark

* Corresponding author

E-mail: h.yazdanian@kntu.ac.ir

July 2021

Abstract. This paper focuses on conductivity imaging of a three dimensional object using interior current density information (ICDI). Applications include the emerging hybrid tomographic methods known as magnetic resonance electrical impedance tomography and current density impedance imaging, which potentially have both high contrast and high resolution. For all possible forms of ICDI data, the Fréchet derivative of the map between conductivity and ICDI is derived. Then, an iterative reconstruction method is formulated based on the Newton scheme. The method is implemented numerically and its properties are investigated on simulated data obtained from two different phantoms. The method is also benchmarked against the J -substitution method. We systematically study the possibilities, challenges, shortcomings, and artifacts due the different forms of full and partial ICDI data and one or several boundary conditions. The results establish that at least two components of two non-parallel interior current densities are required to obtain good reconstructions; this is an important outcome for conductivity imaging methods which use only one component of the magnetic field. The results hold promise for the near real-time and high resolution conductivity reconstruction in practical applications.

Keywords: conductivity imaging, hybrid tomography, Newton algorithm, partial data

1. Introduction

High resolution and contrast information about the electrical conductivity distribution inside biological tissues, obtained noninvasively, is of high interest for a wide range of medical applications. Early diagnosis of breast cancer [1], EEG source localization [2], and targeting control in transcranial brain stimulation [3] are among the most studied examples of these applications. Electrical impedance tomography (EIT) is the most well-known method for conductivity imaging. The mathematical formulation of EIT is governed by the generalized Laplace equation with the Dirichlet boundary condition

$$\begin{aligned} \nabla \cdot \sigma \nabla u &= 0 && \text{in } \Omega, \\ u &= f && \text{on } \partial\Omega, \end{aligned} \tag{1}$$

where u is the electrical potential caused by an externally applied potential f on the boundary. Here, Ω is an open, bounded subset of \mathbb{R}^3 with sufficiently smooth boundary $\partial\Omega$. The scalar function σ is uniformly bounded from below and above by positive constants.

In EIT, the inverse problem is the reconstruction of σ from knowledge of many pairs of boundary potentials f and corresponding normal boundary currents $\partial_n u|_{\partial\Omega}$; where n denotes the outward unit normal to $\partial\Omega$. Due to diffuse nature of the electric current, the reconstruction problem in EIT is severely ill-posed. To overcome the difficulty, hybrid or coupled-physics techniques for conductivity imaging have been developed recently [4]. The idea is to invoke multiple interacting physical phenomena in a single measurement setup. One particular promising hybrid imaging method, known as magnetic resonance EIT (MREIT), combines the EIT setup with MR imaging [5]. The MR scanner provides information about the interior magnetic field induced by the current field generated by the EIT experiment. This interior information has the potential for a vast improvement of the resolution and contrast in conductivity reconstruction. In practice, only one component of the magnetic field, B_z , is usually available, since measurement of additional components would require undesirable subject rotation inside the MR scanner. Another closely related imaging method called current density impedance imaging (CDII) assumes knowledge of either the interior current field or just its magnitude [6, 7].

In this paper, we consider the reconstruction of the electrical conductivity from interior current density information (ICDI). We ask the question: “How much ICDI data is required in order to obtain a reliable 3D reconstruction of σ with acceptable spatial resolution and contrast?” Our aim is to systematically investigate the use of full or partial ICDI data and how the use of one or several boundary conditions f can compensate for the partial data.

Denote by $\mathbf{J} = -\sigma \nabla u$ the induced interior current field in (1) and by (x, y, z) the Cartesian coordinates in \mathbb{R}^3 . The considered ICDI data is either in the form of the full information, $\mathbf{J} = (J_x, J_y, J_z)$, the magnitude, $|\mathbf{J}| := \sqrt{J_x^2 + J_y^2 + J_z^2}$, two component, $\dot{\mathbf{J}} := (J_x, J_y)$, or one component, $\ddot{\mathbf{J}} := J_x$. In terms of (1), the different forms of ICDI inside Ω are given by

$$\mathbf{J} = -\left(\sigma \frac{\partial u}{\partial x}, \sigma \frac{\partial u}{\partial y}, \sigma \frac{\partial u}{\partial z}\right), \quad (2a)$$

$$|\mathbf{J}| = \sigma \sqrt{\left(\frac{\partial u}{\partial x}\right)^2 + \left(\frac{\partial u}{\partial y}\right)^2 + \left(\frac{\partial u}{\partial z}\right)^2}, \quad (2b)$$

$$\dot{\mathbf{J}} = -\left(\sigma \frac{\partial u}{\partial x}, \sigma \frac{\partial u}{\partial y}\right), \quad (2c)$$

$$\ddot{\mathbf{J}} = -\sigma \frac{\partial u}{\partial x}. \quad (2d)$$

The reconstruction problem is now as follows: Given the ICDI data possibly for several choices of boundary potentials f , reconstruct the conductivity distribution σ . The motivation for studying the particular partial data (2c) is that the component B_z of the magnetic field usually measured in MREIT carries no information about J_z . Thus our investigations may pave the way for an MREIT approach through the steps $B_z \mapsto \dot{\mathbf{J}} \mapsto \sigma$. We are also especially interested in assessing the minimum number of interior measurements which are required to obtain a good reconstruction for the

particular partial data (2c).

Existing reconstruction algorithms in the literature can be divided into the direct (or non-iterative) and iterative methods. Ider and Birgul [8] used a perturbation method and linearized the problem to reconstruct 2D conductivity for simple phantoms. This direct method uses the full \mathbf{J} . The non-iterative equipotential line method was proposed in [9] to uniquely recover σ in 2D. This approach is based on the fact that the current lines and the equipotential lines are perpendicular to each other. The method uses one measurement of the full \mathbf{J} . A similar approach has been adopted in [10]. In [11], the problem of recovering the conductivity from knowledge of at least two magnitude of non-parallel currents, $|\mathbf{J}|$, was treated as a hyperbolic system of first order partial differential equations (PDEs), and three numerical methods were given for its solution. Joy et al. [12] and Lee [13] independently discovered a simple explicit reconstruction formula which uses two transversal \mathbf{J} measurements and determines the σ up to a multiplicative constant. In [6, 14], this method was validated by 3D phantoms and experimental data.

One of the most well-known iterative reconstruction algorithms is the J -substitution method proposed in [15]. This method considers conductivity reconstruction from at least two magnitudes of non-parallel current densities inside the domain. In [16, 17] the existence and uniqueness of the mathematical model were proved and the convergence of the algorithm was studied. The algorithm was subsequently considered in other works [18, 19] to reconstruct conductivity in 3D. In [20], J -substitution method was extended to handle projected current density data acquired from B_z measurements, see also [21]. In [7, 22, 23], $|\mathbf{J}|$ has been used to iteratively reconstruct conductivity in 2D.

The mathematical theory for imaging with ICDI data is fairly complete for data of the form (2a) and (2b). Uniqueness and stability was established in [24] for one measurement of magnitude data (2b). The method of proof relies on a transition from the linearized problem to the non-linear problem; in some sense this approach forms the foundation for our numerical method for this kind of data. We note, however, that no mathematical results for imaging with data of the form (2c) and (2d) seem to be available in the literature. See also [25, 26] for more on the mathematics of hybrid data inverse problems.

We consider for the first time a Newton iterative scheme for conductivity reconstruction in 3D. Our method is similar to the approach found in [27, 28] for the 2D problem, however, we here develop the method for all forms of ICDI data. The uniform approach allows us to systematically study the possibilities, challenges, shortcomings, and artifacts due the different forms of full and partial ICDI data. We evaluate the approach by the simulated data through two numerical phantoms.

This paper is organized as follows: in Section 2, we first derive the Fréchet derivative of the forward map, next we present the reconstruction problem as a collection of linear PDE problems, and then we explain the Newton iterative scheme. In Section 3, the numerical implementation of the forward and inverse problems will be presented. In Section 4, the developed algorithm will be evaluated through using two numerical phantoms. In this section, we numerically study the conductivity reconstruction due the different forms of full and partial ICDI data and one or several boundary conditions. Next, a noise study is presented, and then the Newton algorithm is evaluated in comparison with the J -substitution method in this section. Finally, Section 5 presents the conclusions.

2. Methods

The reconstruction problem is properly cast in terms of the forward mappings

$$\mathcal{F} : \sigma \mapsto \mathbf{J}, \quad (3a)$$

$$|\mathcal{F}| : \sigma \mapsto |\mathbf{J}|, \quad (3b)$$

$$\dot{\mathcal{F}} : \sigma \mapsto \dot{\mathbf{J}}, \quad (3c)$$

$$\ddot{\mathcal{F}} : \sigma \mapsto \ddot{\mathbf{J}}, \quad (3d)$$

corresponding to the different kinds of ICDI data (2). We first work with one boundary condition and eventually expand to several. To establish the functional space setting, let $L_+^\infty(\Omega)$ denote the space of functions in Ω bounded below and above by positive constants ν and μ , respectively. The constants are assumed to be known as a priori in our procedure below. When f is sufficiently regular, the maps defined by (3) can be considered as a mappings $L_+^\infty(\Omega) \mapsto [L^2(\Omega)]^i$, with $i = 1, 2, 3$ denoting the number of components in the data. Our exposition focuses on the inverse problem for (3a): Given data \mathbf{J} , solve for σ the non-linear functional equation

$$\mathcal{F}(\sigma) = \mathbf{J}. \quad (4)$$

We propose a Newton scheme for approximating a solution to the equation. Therefore, below in Section 2.1, we first compute the Fréchet derivative of the forward maps. Then, we setup the linear system to replace (4). Finally in Section 2.3, we state the Newton iterative scheme to solve the inverse problem.

2.1. The Fréchet derivative

Let \tilde{u} be the unique solution to (1) when σ is replaced by the reference conductivity $\tilde{\sigma}$. We assume that $\tilde{\sigma}$ and f are sufficiently smooth thus making the reference potential \tilde{u} sufficiently regular by elliptic regularity.

For $\delta\sigma$ in a class of admissible variations, we look for a linear operator, $d\mathcal{F}(\tilde{\sigma})$, that resembles the Fréchet derivative of \mathcal{F} around $\tilde{\sigma}$ in the direction $\delta\sigma$, i.e. the first order approximation

$$\mathcal{F}(\tilde{\sigma} + \delta\sigma) - \mathcal{F}(\tilde{\sigma}) \approx d\mathcal{F}(\tilde{\sigma})\delta\sigma \quad (5)$$

is valid with the precise estimate

$$\|\mathcal{F}(\tilde{\sigma} + \delta\sigma) - \mathcal{F}(\tilde{\sigma}) - d\mathcal{F}(\tilde{\sigma})\delta\sigma\|_{L^2(\Omega)} \leq c\|\delta\sigma\|_{L^\infty(\Omega)}^2$$

for some positive constant c independent of $\delta\sigma$. One can show that the derivative is given by

$$d\mathcal{F}(\tilde{\sigma})\delta\sigma = -\delta\sigma\nabla\tilde{u} - \tilde{\sigma}\nabla\delta u, \quad (6)$$

where $\delta u \in H_0^1(\Omega)$ solves

$$\begin{aligned} \nabla \cdot \tilde{\sigma}\nabla\delta u &= -\nabla \cdot \delta\sigma\nabla\tilde{u}, & \text{in } \Omega, \\ \delta u &= 0, & \text{on } \partial\Omega. \end{aligned} \quad (7)$$

Here, $H_0^1(\Omega)$ denotes the Sobolev space of weakly differentiable functions with vanishing boundary trace.

The Fréchet derivative defined by (6) is a vector-valued function. Thus, when \mathbf{J} or $\ddot{\mathbf{J}}$ is available, only the corresponding components of (6) enter in the linearization. However, when $|\mathbf{J}|$ is available, the Fréchet derivative is in the following form [27, 28]

$$d|\mathcal{F}|(\tilde{\sigma})\delta\sigma = |\nabla\tilde{u}|\delta\sigma + \tilde{\sigma}\frac{\nabla\tilde{u} \cdot \nabla\delta u}{|\nabla\tilde{u}|}. \quad (8)$$

Knowing that $|\mathbf{J}| = \sigma|\nabla u| = -\mathbf{J} \cdot \nabla u / |\nabla u|$, (8) is obtained by taking the inner product of (6) with $-\nabla\tilde{u}/|\nabla\tilde{u}|$.

The Fréchet derivative for the various forms of ICDI can be written as follows:

$$d\mathcal{F}(\tilde{\sigma})\delta\sigma = -\left(\delta\sigma\frac{\partial\tilde{u}}{\partial x}, \delta\sigma\frac{\partial\tilde{u}}{\partial y}, \delta\sigma\frac{\partial\tilde{u}}{\partial z}\right) - \left(\tilde{\sigma}\frac{\partial\delta u}{\partial x}, \tilde{\sigma}\frac{\partial\delta u}{\partial y}, \tilde{\sigma}\frac{\partial\delta u}{\partial z}\right), \quad (9a)$$

$$d|\mathcal{F}|(\tilde{\sigma})\delta\sigma = |\nabla\tilde{u}|\delta\sigma + \tilde{\sigma}\frac{\nabla\tilde{u} \cdot \nabla\delta u}{|\nabla\tilde{u}|}, \quad (9b)$$

$$d\dot{\mathcal{F}}(\tilde{\sigma})\delta\sigma = -\left(\delta\sigma\frac{\partial\tilde{u}}{\partial x}, \delta\sigma\frac{\partial\tilde{u}}{\partial y}\right) - \left(\tilde{\sigma}\frac{\partial\delta u}{\partial x}, \tilde{\sigma}\frac{\partial\delta u}{\partial y}\right), \quad (9c)$$

$$d\ddot{\mathcal{F}}(\tilde{\sigma})\delta\sigma = -\delta\sigma\frac{\partial\tilde{u}}{\partial x} - \tilde{\sigma}\frac{\partial\delta u}{\partial x}. \quad (9d)$$

2.2. The linear system of PDEs

We obtain the linearized problem by replacing $\mathcal{F}(\tilde{\sigma} + \delta\sigma)$ with the ICDI data \mathbf{J} in (5) as follows:

$$d\mathcal{F}(\tilde{\sigma})\delta\sigma = \mathbf{J} - \mathcal{F}(\tilde{\sigma}). \quad (10)$$

This equation is in fact a system of equations that by considering (6) and (7) can be stated in the matrix form

$$\begin{bmatrix} \nabla \cdot ([\cdot]\nabla\tilde{u}) & \nabla \cdot (\tilde{\sigma}\nabla[\cdot]) \\ -\nabla\tilde{u} & -\tilde{\sigma}\nabla[\cdot] \end{bmatrix} \begin{bmatrix} \delta\sigma \\ \delta u \end{bmatrix} = \begin{bmatrix} 0 \\ \mathbf{J} - \mathcal{F}(\tilde{\sigma}) \end{bmatrix}. \quad (11)$$

It is noteworthy that the second equation in (11) contains three components and can be expressed as three scalar equations in the expanded form. If ICDI data is in the form of $\dot{\mathbf{J}}$, then the second equation of (11) includes x and y components. If ICDI data is in the form of $\ddot{\mathbf{J}}$, then the second equation of (11) only includes x component. If ICDI data is in the form of $|\mathbf{J}|$, then

$$\begin{bmatrix} \nabla \cdot ([\cdot]\nabla\tilde{u}) & \nabla \cdot (\tilde{\sigma}\nabla[\cdot]) \\ |\nabla\tilde{u}| & \tilde{\sigma}\frac{\nabla\tilde{u} \cdot \nabla[\cdot]}{|\nabla\tilde{u}|} \end{bmatrix} \begin{bmatrix} \delta\sigma \\ \delta u \end{bmatrix} = \begin{bmatrix} 0 \\ |\mathbf{J}| - |\mathcal{F}|(\tilde{\sigma}) \end{bmatrix}. \quad (12)$$

The system is in all forms equipped with a homogeneous Dirichlet boundary condition imposed on δu .

So far we have assumed that ICDI is available for one boundary condition. Now consider the set of M ICDI data, \mathbf{J}_m , $1 \leq m \leq M$, realized by applying M electrical potential patterns on the boundary $\partial\Omega$, f_m , $1 \leq m \leq M$. Along the same lines, (11) now generalizes to the coupled system of equations in the matrix form

$$\mathbf{A}\mathbf{x} = \mathbf{b}, \quad (13)$$

where

$$\mathbf{A} = \begin{bmatrix} \nabla \cdot ([\cdot] \nabla \tilde{u}_1) & \nabla \cdot (\tilde{\sigma} \nabla [\cdot]) & \cdots & 0 \\ \vdots & \vdots & \ddots & \vdots \\ \nabla \cdot ([\cdot] \nabla \tilde{u}_M) & 0 & \cdots & \nabla \cdot (\tilde{\sigma} \nabla [\cdot]) \\ -\nabla \tilde{u}_1 & -\tilde{\sigma} \nabla [\cdot] & \cdots & 0 \\ \vdots & \vdots & \ddots & \vdots \\ -\nabla \tilde{u}_M & 0 & \cdots & -\tilde{\sigma} \nabla [\cdot] \end{bmatrix}, \quad \mathbf{x} = \begin{bmatrix} \delta \sigma \\ \delta u_1 \\ \vdots \\ \delta u_M \end{bmatrix}, \quad \mathbf{b} = \begin{bmatrix} 0 \\ \vdots \\ 0 \\ \mathbf{J}_1 - \mathcal{F}_1(\tilde{\sigma}) \\ \vdots \\ \mathbf{J}_M - \mathcal{F}_M(\tilde{\sigma}) \end{bmatrix}. \quad (14)$$

As noted above, the Fréchet derivative terms in (14) have three components. If ICDI data is in the form of $\dot{\mathbf{J}}_m$, then the first two components are used in (14). If ICDI data is in the form of $\ddot{\mathbf{J}}_m$, then only the first component of those terms is used in (14). If ICDI data is in the form of $|\mathbf{J}_m|$, then the matrices in (13) would be as follows:

$$\mathbf{A} = \begin{bmatrix} \nabla \cdot ([\cdot] \nabla \tilde{u}_1) & \nabla \cdot (\tilde{\sigma} \nabla [\cdot]) & \cdots & 0 \\ \vdots & \vdots & \ddots & \vdots \\ \nabla \cdot ([\cdot] \nabla \tilde{u}_M) & 0 & \cdots & \nabla \cdot (\tilde{\sigma} \nabla [\cdot]) \\ |\nabla \tilde{u}_1| & \tilde{\sigma} \frac{\nabla \tilde{u}_1 \cdot \nabla [\cdot]}{|\nabla \tilde{u}_1|} & \cdots & 0 \\ \vdots & \vdots & \ddots & \vdots \\ |\nabla \tilde{u}_M| & 0 & \cdots \tilde{\sigma} \frac{\nabla \tilde{u}_M \cdot \nabla [\cdot]}{|\nabla \tilde{u}_M|} & \end{bmatrix}, \quad \mathbf{x} = \begin{bmatrix} \delta \sigma \\ \delta u_1 \\ \vdots \\ \delta u_M \end{bmatrix}, \quad \mathbf{b} = \begin{bmatrix} 0 \\ \vdots \\ 0 \\ |\mathbf{J}_1| - |\mathcal{F}_1|(\tilde{\sigma}) \\ \vdots \\ |\mathbf{J}_M| - |\mathcal{F}_M|(\tilde{\sigma}) \end{bmatrix}. \quad (15)$$

The system of linear PDEs (13) is equipped with homogeneous Dirichlet boundary conditions imposed on δu_m , $1 \leq m \leq M$.

When the full \mathbf{J}_m is used, (13) consists of $4M$ scalar equations and $M + 1$ scalar unknowns. It means that the system is formally overdetermined for $M \geq 1$. When $\dot{\mathbf{J}}_m$ is used, (13) includes $3M$ scalar equations and $M + 1$ scalar unknowns. Again, it means that the system is formally overdetermined for $M \geq 1$. When $\ddot{\mathbf{J}}_m$ or $|\mathbf{J}_m|$ is used, (13) includes $2M$ scalar equations and $M + 1$ scalar unknowns. It means that the system is formally determined for $M = 1$ and overdetermined for $M > 1$.

2.3. The Newton scheme

In this section, an iterative Newton-type algorithm is employed to approximately solve (13). As discussed before, (13) is an overdetermined system for all $M > 1$. To solve such overdetermined systems, the least squares minimization

$$\mathbf{x}^* = \arg \min_{\mathbf{x}} \|\mathbf{Ax} - \mathbf{b}\|_{L^2(\Omega)}^2 \quad (16)$$

is a standard approach. Here, the appropriate function space is $\mathbf{x} \in H^1(\Omega) \times [H_0^1(\Omega) \cap H^2(\Omega)]^{i \times M}$, with $i = 1, 2, 3$ denoting the number of components in the data.

In the Newton scheme we simply iterate the above:

Algorithm: Newton iteration for conductivity reconstruction by ICDI

Data: Simulated \mathbf{J}_m , $1 \leq m \leq M$.

Inputs: $\sigma^0 = \tilde{\sigma}$ (initial guess);
 M (number of measurements);
 K (maximum number of iterations);
 T (tolerance level);
 ν and μ (lower and upper bounds of σ).

Initialization: Choose ICDI type (\mathbf{J}_m , $|\mathbf{J}_m|$, $\dot{\mathbf{J}}_m$, or $\ddot{\mathbf{J}}_m$);
Set $k = 0$ and $\epsilon^0 = 2T$.

```

while  $k < K$  and  $\epsilon^k > T$  do
    for  $(m = 1, \dots, M)$  do
        | Solve for  $u_m^k$  in  $\begin{cases} \nabla \cdot \sigma^k \nabla u_m^k = 0 & \text{in } \Omega, \\ u_m^k = f_m & \text{on } \partial\Omega. \end{cases}$ 
    end
    Set-up  $\mathbf{A}$  and  $\mathbf{b}$  ( $u_m^k = \tilde{u}_m$  and  $\sigma^k = \tilde{\sigma}$ ) based on the available ICDI.
    Find  $\mathbf{x}^* = \arg \min_{\mathbf{x}} \|\mathbf{Ax} - \mathbf{b}\|_{L^2(\Omega)}^2$ .
    Extract  $\delta\sigma^k$  from  $\mathbf{x}^*$ .
    Update  $\sigma^{k+1} = P(\sigma^k + \delta\sigma^k)$ .
    Constrain the conductivity map:  $\sigma^{k+1} = \begin{cases} \max(\nu, \sigma^{k+1}) \\ \min(\mu, \sigma^{k+1}). \end{cases}$ 
    Set  $\epsilon^k = \|\delta\sigma^k\|_{L^2(\Omega)}$  and  $k = k + 1$ .
end

```

Here, σ^k is the approximated conductivity at k 'th iteration and u_m^k is the corresponding potential. The solution of the forward problem at the k 'th iteration enters in \mathbf{b} ; it is obtained from (2) with σ replaced by σ^k . The operator P projects the update to a space of sufficiently smooth functions allowing the iteration to continue. This operation is not required in the finite dimensional implementation though, since the computed function is already regular. A constraint is applied to σ^{k+1} to fit the values to the interval $[\nu, \mu]$. It guarantees that σ^{k+1} satisfied the required assumptions. The iteration stops when either a maximum number of iterations (K) is reached, or when the update $\epsilon^k = \|\delta\sigma^k\|_{L^2(\Omega)}$ is smaller than the threshold T . For the $|\mathbf{J}_m|$ form, this algorithm is almost similar to the 2D work in [27].

3. Numerical settings and implementation details

In this section, we present implementation details of the algorithm in Python 3 using the FEniCS package [29], a collection of free softwares with an extensive list of features for automated, efficient solving of partial differential equations. To this end, we first derive variational formulations for the forward and inverse problems which are directly implementable in FEniCS. Then, we introduce phantoms used for numerical experiments and then present other numerical settings. For all visualizing purposes, we use the open-source visualization software Paraview [30].

3.1. The forward problem

The forward problem is implemented to generate the right hand side of (13), \mathbf{b} , and the gradients of the potentials, ∇u_m^k , at the k 'th iteration. We obtain these by implementing the weak form of (1) in FEniCS.

3.2. Variational form of the linearised inverse problem

As noted in Section 2.3, we use the method of least squares minimization to solve the linearised inverse problem (13). Thus, we employ the least square finite element (LSFEM) [31] to formulate an appropriate numerical method for solving (13).

For numerical implementation, we transform the second order least squares problem (16) into a first order problem [27]. In this way, we obtain the new minimization problem

$$\arg \min_{\mathbf{x}, \hat{\mathbf{x}}} \left(\|\hat{\mathbf{A}}\hat{\mathbf{x}} - \mathbf{b}\|_{L^2(\Omega)}^2 + \|\mathbf{G}\mathbf{x} - \hat{\mathbf{x}}\|_{L^2(\Omega)}^2 \right), \quad (17)$$

where $\mathbf{G} = \text{diag}(1, \nabla, \dots, \nabla)$, $\mathbf{G}\mathbf{x} = \hat{\mathbf{x}}$, and $\mathbf{A} = \hat{\mathbf{A}}\mathbf{G}$. The operator \mathbf{G} essentially transforms the variable δu_m^k to its gradient, such that $\hat{\mathbf{A}}$ is a first order operator.

Since the operators $\hat{\mathbf{A}} : H_0^1(\Omega) \times [H_{\text{div}}(\Omega)]^{i \times M} \rightarrow [L^2(\Omega)]^{i \times 2M}$, with $i = 1, 2, 3$ denoting the number of components in vector fields, and $\mathbf{G} : H_0^1(\Omega) \times [H^1(\Omega)]^M \rightarrow [H^1(\Omega)] \times [L^2(\Omega)]^M$, the appropriate function space for $(\mathbf{x}, \hat{\mathbf{x}})$ is

$$\mathcal{X} = H^1(\Omega) \times [H_0^1(\Omega)]^M \times H^1(\Omega) \times [H_{\text{div}}(\Omega)]^{i \times M}.$$

Here $H_{\text{div}}(\Omega)$ denotes the usual (Hilbert) space of vector functions in $[L^2(\Omega)]^3$ for which the divergence is also an $L^2(\Omega)$ function. Note that the implicit homogeneous Dirichlet boundary conditions for δu_m^k , $1 \leq m \leq M$, are imposed by the chosen function spaces $H_0^1(\Omega)$. The weak formulation of (17) is now: Find $\{\mathbf{x}, \hat{\mathbf{x}}\} \in \mathcal{X}$ such that

$$\int_{\Omega} \left[(\hat{\mathbf{A}}\hat{\mathbf{x}})^T \hat{\mathbf{A}}\hat{\mathbf{v}} + (\mathbf{G}\mathbf{x} - \hat{\mathbf{x}})^T (\mathbf{G}\mathbf{v} - \hat{\mathbf{v}}) \right] dV = \int_{\Omega} \mathbf{b}^T \hat{\mathbf{A}}\hat{\mathbf{v}} dV \quad (18)$$

$$\forall \{\mathbf{v}, \hat{\mathbf{v}}\} \in \mathcal{X}.$$

In the finite dimensional setting, we use conforming first order continuous Galerkin (CG1) elements for $\delta \sigma^k$ and δu_m^k and conforming first order Raviart-Thomas (RT1) elements for $\nabla \delta u_m^k$ [29]. The problem (17) is potentially ill-posed. In that case a Tikhonov regularization term $\alpha \|\mathbf{x}\|_{L^2(\Omega)}^2$ is added to (17). The weak formulation (18) then becomes

$$\int_{\Omega} \left[(\hat{\mathbf{A}}\hat{\mathbf{x}})^T \hat{\mathbf{A}}\hat{\mathbf{v}} + (\mathbf{G}\mathbf{x} - \hat{\mathbf{x}})^T (\mathbf{G}\mathbf{v} - \hat{\mathbf{v}}) + \alpha \mathbf{x}^T \mathbf{v} \right] dV = \int_{\Omega} \mathbf{b}^T \hat{\mathbf{A}}\hat{\mathbf{v}} dV \quad (19)$$

$$\forall \{\mathbf{v}, \hat{\mathbf{v}}\} \in \mathcal{X}$$

where $\alpha > 0$ is a regularization parameter.

3.3. Geometry, phantoms, and mesh

To simplify the implementation and meshing, a cubic domain Ω is considered. We will study two different 3D phantoms: a simple phantom as shown in Figure 1a and

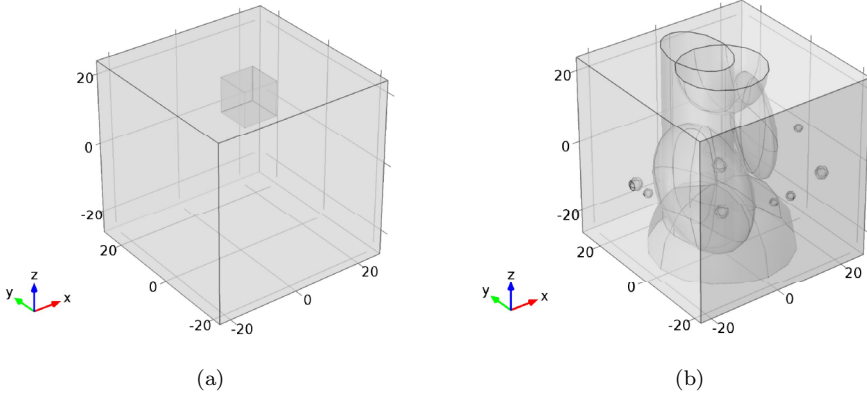


Figure 1: (a) Simple phantom and (b) Complex phantom used in numerical experiments. Information about phantoms is presented in the text. All dimensions are in mm.

a complex phantom as shown in Figure 1b. The simple phantom is embedded in a 50 mm cube with the origin at its centre and the conductivity of 1×10^{-3} S/mm. A cubic inclusion with side length of 10 mm and the conductivity of 1.5×10^{-3} S/mm is centered at (10, 10, 10) mm. This phantom is chosen because it is relatively simple to implement and it is easy to assess the reconstruction quality. Moreover, it reveals how streaking artifacts obtained from solving a linearized problem may appear (as found in 2D [28]). The phantom is implemented by a function in FEniCS and then projected on a CG1 space.

The complex phantom is embedded in a 50 mm cube with the origin at its centre and is constructed as [32]. It is a three-dimensional modification of the well-known Shepp–Logan head phantom [33]. The conductivity distribution includes thirteen different ellipsoidal and one cylindrical regions with different conductivity values and there is no symmetry in any direction as shown in Table 1. We chose this phantom to evaluate the algorithm in a more realistic situation. The phantom is implemented by a function in FEniCS and then projected on a CG1 space.

Both phantoms were automatically meshed by uniform tetrahedral elements using the FEniCS package. To avoid committing an inverse crime, different meshes have been used for generating simulated data and reconstruction. An overview of the characteristics of meshes is given in Table 2.

3.4. Other details

The finite element system of equations give very large sparse matrices for both phantoms. To handle such large problems, we run the code in parallel using Message Passing Interface (MPI) which is supported by FEniCS (OpenMPI, mpi/3.1.5-gcc/8.3.0). Furthermore, iterative solvers are preferred to solve the very large sparse system of equations over direct solvers. Various iterative solvers are available in FEniCS. We tested different preconditioned Krylov solvers, which could be used in parallel (PETScKrylovSolver, petsc-3.10.5). Among them, biconjugate gradient

Table 1: Details of the complex phantom

Object	Radius (mm)			Centre (mm)			Rotation angle (°)	Conductivity $\times 10^{-3}$ (S/mm)
	r_x	r_y	r_z	x	y	z		
Ellipsoid 1	1.9	1.9	1.9	-2.5	-2.5	0.0	0.0	2.0
Ellipsoid 2	1.9	1.9	1.9	0.0	5.0	0.0	0.0	2.0
Ellipsoid 3	1.7	1.7	1.7	15.0	-20.0	0.0	0.0	2.0
Ellipsoid 4	1.7	1.7	1.7	-15.0	-20.0	0.0	0.0	2.0
Ellipsoid 5	1.2	1.2	1.2	2.5	-23.8	0.0	0.0	1.5
Ellipsoid 6	1.2	1.2	1.2	-2.5	-23.8	0.0	0.0	2.0
Ellipsoid 7	1.2	1.2	1.2	-23.8	-2.5	0.0	0.0	2.0
Ellipsoid 8	1.7	1.7	1.7	-23.8	2.5	0.0	0.0	2.0
Ellipsoid 9	1.2	1.2	1.2	23.8	0.0	0.0	0.0	1.5
Ellipsoid 10	13.4	3.4	13.4	7.5	-2.5	7.5	75.0	0.1
Ellipsoid 11	15.5	5.3	17.7	-7.5	-2.5	-5.0	105.0	0.1
Ellipsoid 12	11.3	11.3	11.3	0.0	0.0	25.0	0.0	1.0
Ellipsoid 13	18.8	18.8	18.8	0.0	0.0	25.0	0.0	1.5
Cylinder	7.5	11.3	NA	0.0	10.0	NA	0.0	1.0
Background	NA	NA	NA	NA	NA	NA	NA	0.5

Table 2: Mesh

Phantom	mesh purpose	Nodes ($\times 10^6$)	Tetrahedra ($\times 10^6$)
Simple	Data	0.75	4.37
	Reconstruction	0.70	4.10
Complex	Data	1.77	10.37
	Reconstruction	1.69	9.86

stabilized (bicgstab) solver with successive over relaxation (sor) preconditioner has shown the best performance in terms of run-time and convergence. The results below are all computed with this solver.

To study the convergence characteristics of the algorithm, we define the relative L^2 -error of a reconstructed conductivity image in each iteration k as

$$E_k(\%) = \frac{\|\sigma_{\text{true}} - \sigma^k\|_{L^2(\Omega)}}{\|\sigma_{\text{true}}\|_{L^2(\Omega)}} \quad (20)$$

where $\|\cdot\|_{L^2(\Omega)}$ denotes the L^2 -norm and σ_{true} is the true conductivity distribution. The error is computed with FEniCS on the reconstruction mesh.

In order to study the robustness of the algorithm when partial ICDI is used, we add different levels of the additive white Gaussian noise to the exact interior data. As an example, when the interior data is \mathbf{J}_m , the noise is added in the following way:

$$\mathbf{J}_m^\delta = \mathbf{J}_m + \delta \frac{\mathbf{n}_m}{\|\mathbf{n}_m\|_{L^2(\Omega)}} \|\mathbf{J}_m\|_{L^2(\Omega)}, \quad (21)$$

where \mathbf{J}_m^δ and \mathbf{n}_m are the noisy interior data and a noise vector for m 'th measurement, respectively, and δ is the relative noise level; i.e., $\delta = \|\mathbf{n}_m\|_{L^2(\Omega)}/\|\mathbf{J}_m\|_{L^2(\Omega)}$. The elements of \mathbf{n}_m are i.i.d Gaussian random variable with mean 0 and variance 1.

We use a fixed number K to terminate the iteration. However, in practice where monitoring the error in the reconstructed conductivity image is not possible, it is crucial to use other stopping criteria, as well.

4. Numerical results

In this section, by using both simple and complex phantoms, we design various numerical experiments to answer the following questions:

- What is the minimum ICDI required for a reasonable 3D reconstruction of σ ?
- What artifacts are observed in the reconstruction?
- How does the algorithm work for a complex and large scale problem?
- What is the robustness of the algorithm against noise?
- How does our results and method compare to other reconstruction algorithms?

In Section 4.1, we try to answer the first two questions using the simple phantom and through three numerical experiments. Next, by building on the findings in Section 4.1, we will answer the third question in Section 4.2. Then, we answer the fourth question in Section 4.3. Finally, by implementing the J -substitution method in Section 4.4, we answer the last question.

For all simulations, the initial conductivity value is chosen as $\sigma^0 = 0.5 \times 10^{-3}$ S/mm. Moreover, the lower (ν) and upper (μ) bounds on the reconstructed conductivity in each iteration are set to 10^{-7} and 3×10^{-3} S/mm, respectively, in all experiments. All simulations are executed on an HPC system with 24 cores.

4.1. Simple phantom

In this subsection, the results for the simple phantom are presented. We consider three cases, Case A, Case B, and Case C, as shown in Table 3. For Case A, one interior measurement ($M = 1$) corresponding to the imposed boundary condition $f_1 = x$ is available. For Case B, two interior measurements ($M = 2$) corresponding to the imposed boundary conditions $f_1 = x$ and $f_2 = y$ are available. For Case C, three interior measurements ($M = 3$) corresponding to the imposed boundary conditions $f_1 = x$, $f_2 = y$, and $f_3 = z$ are available. The boundary conditions are chosen in such a way that make the interior current fields non-parallel at least in the first iteration when σ_0 is constant. For each case, four ICDI forms, as defined in (2), are used. The following subsections present the results.

Case A: The first row of Figure 2 shows three slices of the true conductivity distribution for (a) the x -axis sliced at 10 mm, (b) the y -axis sliced at 10 mm, and (c) the z -axis sliced at 10 mm. The second to the fifth rows correspond to Case A1, Case A2, Case A3, and Case A4, respectively. The number of iterations was $K = 10$. The elapsed time and required memory were around 2 minutes and 16 GB, respectively. The size of the finite element matrix was about $(1 \cdot 10^7) \times (1 \cdot 10^7)$.

As seen from Figure 2, very good reconstructions are found for the x -axis slices. However, for the other axis slices, the streaking artifacts appear. The boundary

Table 3: Simulations scenarios. M is the number of interior measurements, $m \in [1, M]$, and f is the applied boundary condition.

Case	M	f_m (BCs)	ICDI			
			\mathbf{J}_m	$ \mathbf{J}_m $	$\dot{\mathbf{J}}_m$	$\ddot{\mathbf{J}}_m$
A	1	$f_1 = x$	Case A1	Case A2	Case A3	Case A4
B	2	$f_{1,2} = \{x, y\}$	Case B1	Case B2	Case B3	Case B4
C	3	$f_{1,2,3} = \{x, y, z\}$	Case C1	Case C2	Case C3	Case C4

condition is $f_1 = x$ and the artifacts are perpendicular to the x -axis. Similar artifacts were observed for 2D reconstruction in [28]. The results show that if one is interested in only one slice, only one component of one measurement can produce satisfactory result.

Figure 3 shows the relative L^2 -error of the reconstructed conductivity in each iteration for the various ICDI in Case A. The initial error ($k=0$) was 50%. It means that the error dramatically drops at the first iteration ($k = 1$) and then decreases slowly. The error patterns almost show an exponentially convergence. For all cases, the error is below 2% even after the second iteration.

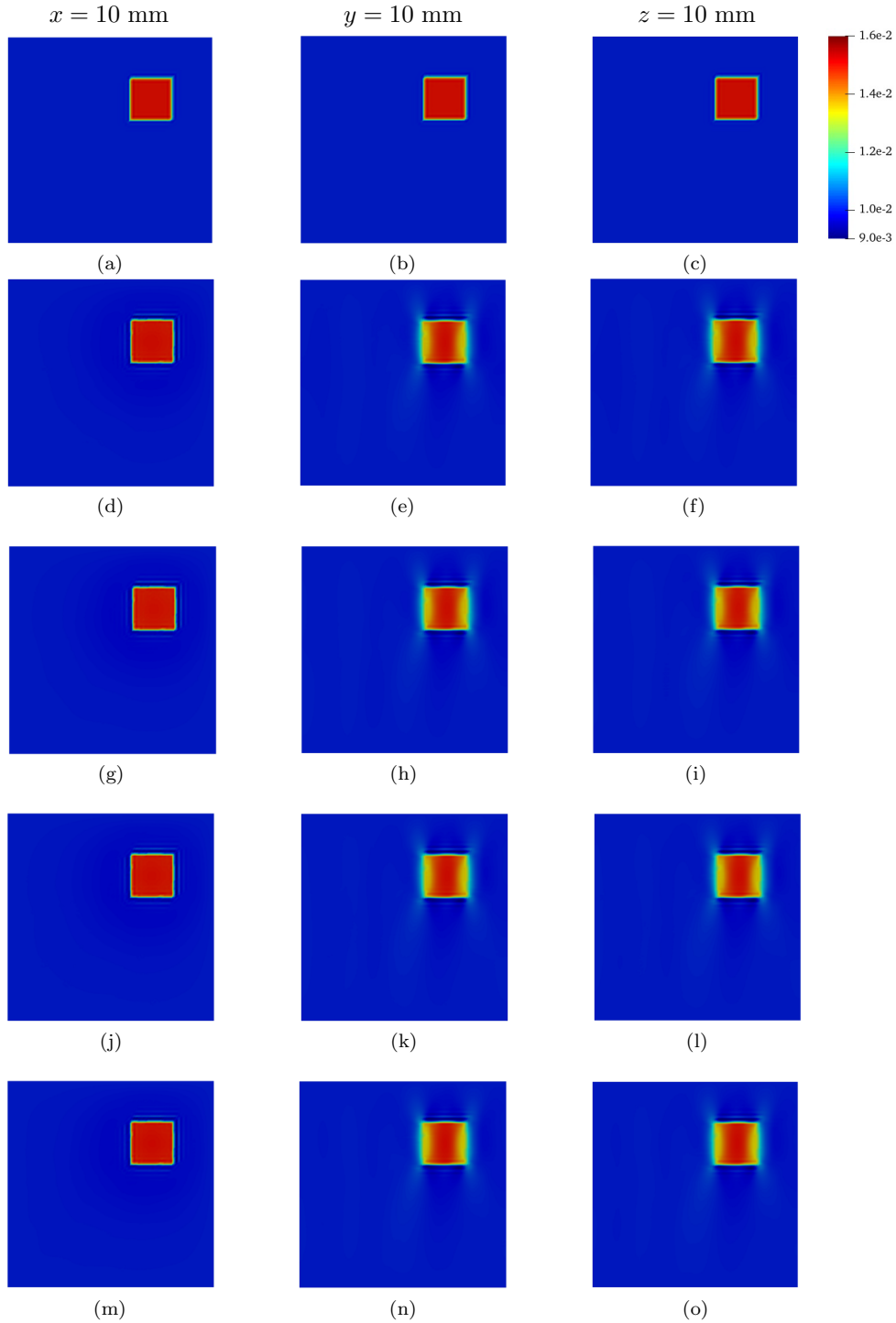


Figure 2: Simple phantom Case A. The first to the third columns correspond to the x -axis sliced at 10 mm, the y -axis sliced at 10 mm, and the z -axis sliced at 10 mm, respectively. The first row is the true conductivity distribution. The second to the fifth rows correspond to Case A1, Case A2, Case A3, and Case A4, respectively. The number of iterations was $K = 10$.

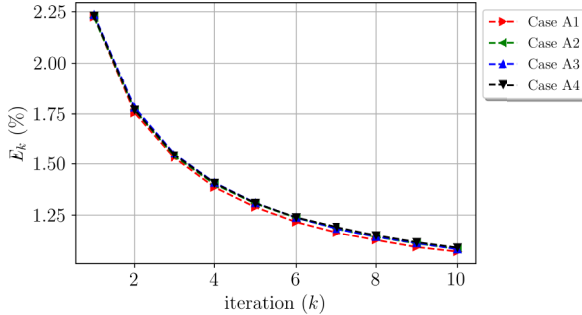


Figure 3: Simple phantom Case A. Relative L^2 -error vs iteration number. The initial error ($k=0$) was 50%.

Case B: The first row of Figure 4 shows three slices of the true conductivity distribution for (a) the x -axis sliced at 10 mm, (b) the y -axis sliced at 10 mm, and (c) the z -axis sliced at 10 mm. The second to the fifth rows correspond to Case B1, Case B2, Case B3, and Case B4, respectively. The number of iterations was $K = 10$. The elapsed time and required memory were around 4 minutes and 34 GB, respectively. The size of the finite element matrix was about $(1.9 \cdot 10^7) \times (1.9 \cdot 10^7)$.

As seen from Figure 4, very good reconstructions are found for Cases B1-B3 in all slices unlike Case A. However, for Case B4, only for the x -axis slice, a very good reconstruction is found. In the y -axis slice (Figure 4n) and the z -axis slice (Figure 4o), artifacts are perpendicular to the x -axis. The result empirically implies that at least two components of two non-parallel interior current densities are required for accurate reconstructions.

Figure 5 shows the relative L^2 -error of the reconstructed conductivity image at each iteration and for the various ICDI in Case B. The initial error ($k=0$) was 50%. In terms of convergence, Case B is similar to Case A. Cases B1-B3 perform almost equally well, however, for Case B4, the error is somewhat larger.

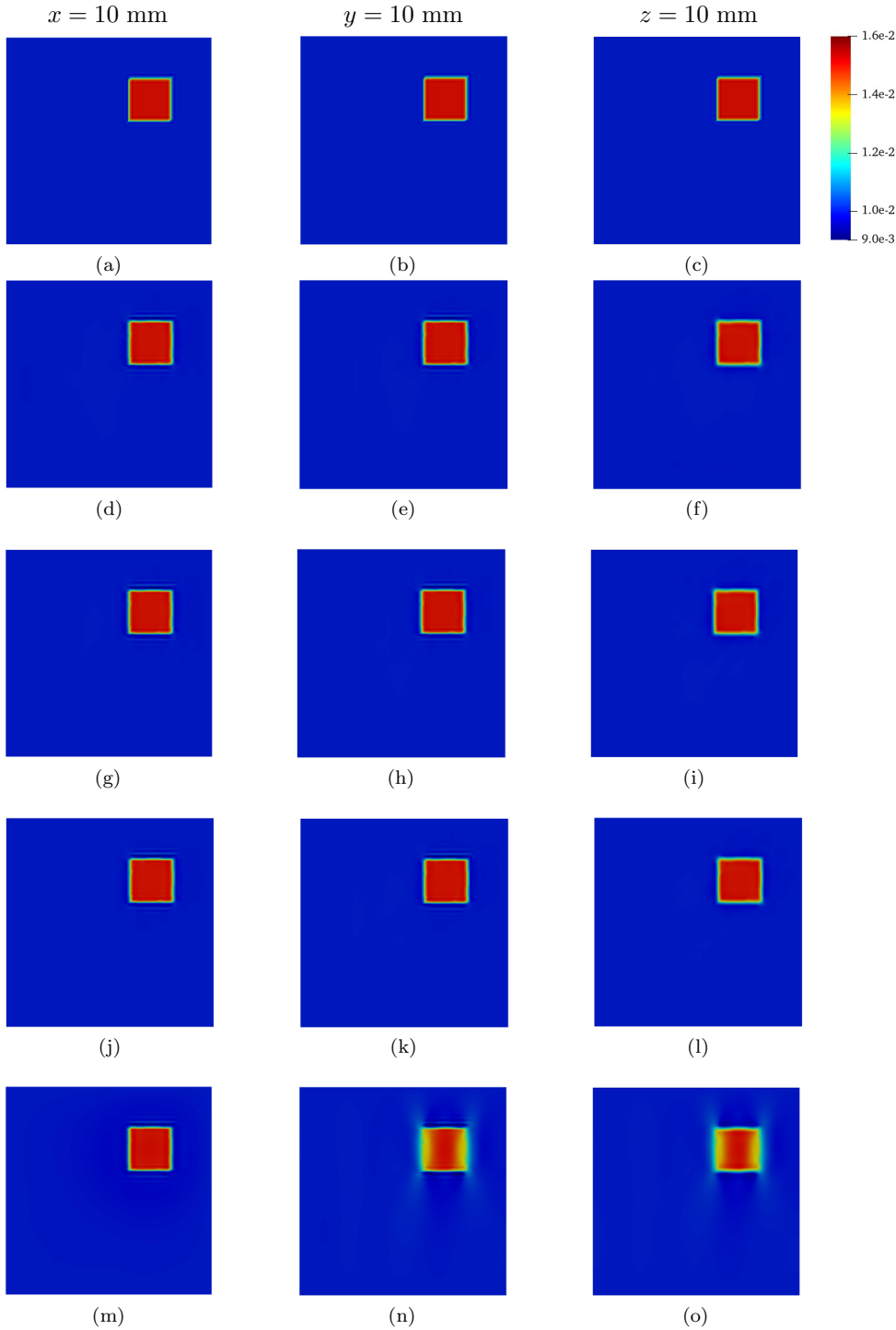


Figure 4: Simple phantom Case B. The first to the third columns correspond to the x -axis sliced at 10 mm, the y -axis sliced at 10 mm, and the z -axis sliced at 10 mm, respectively. The first row is the true conductivity distribution. The second to the fifth rows correspond to Case B1, Case B2, Case B3, and Case B4, respectively. The number of iterations was $K = 10$.

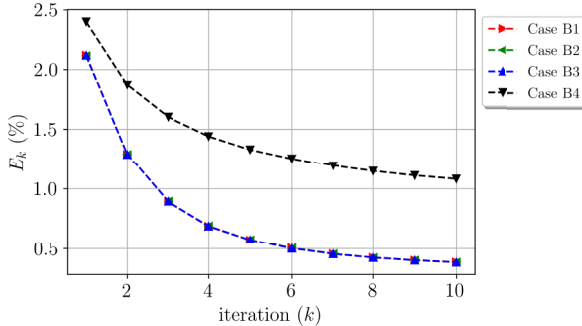


Figure 5: Simple phantom Case B. Relative L^2 -error vs iteration number. The initial error ($k=0$) was 50%.

Case C: The first row of Figure 6 shows three slices of the true conductivity distribution for (a) the x -axis sliced at 10 mm, (b) the y -axis sliced at 10 mm, and (c) the z -axis sliced at 10 mm. The second to the fifth rows correspond to Case C1, Case C2, Case C3, and Case C4, respectively. The number of iterations was $K = 10$. The elapsed time and required memory were around 7 minutes and 55 GB, respectively. The size of the finite element matrix was about $(2.8 \cdot 10^7) \times (2.8 \cdot 10^7)$.

As seen from Figure 6, very good reconstructions are found for Cases C1-C3 in all slices similar to Figure 4. However, for Case C4, again only for the x -axis slice a very good reconstruction is found. In the y -axis slice (Figure 6n) and the z -axis slice (Figure 6o), artifacts are perpendicular to the x -axis. Results empirically imply that even with a sufficient number of interior measurements, the artifacts appear if the proper form of ICDI is not applied.

Figure 7 shows the relative L^2 -error of the reconstructed conductivity image at each iteration and for the various ICDI in Case C. The initial error ($k=0$) was 50%. The trend is similar to the previous cases. Cases B1-B3 perform almost equally well, however, Case B4 stands out with a larger error.

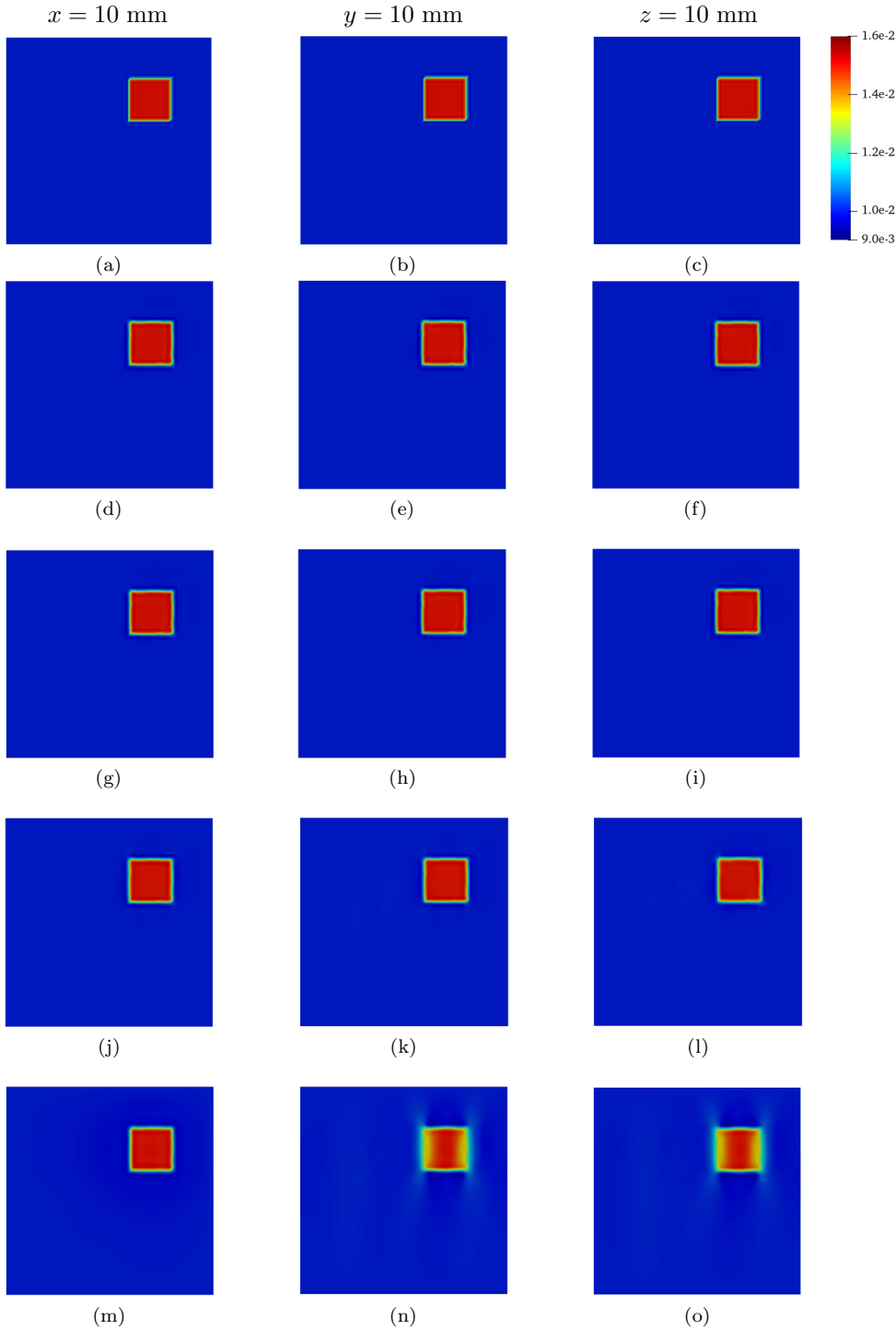


Figure 6: Simple phantom Case C. The first to the third columns correspond to the x -axis sliced at 10 mm, the y -axis sliced at 10 mm, and the z -axis sliced at 10 mm, respectively. The first row is the true conductivity distribution. The second to the fifth rows correspond to Case C1, Case C2, Case C3, and Case C4, respectively. The number of iterations was $K = 10$.

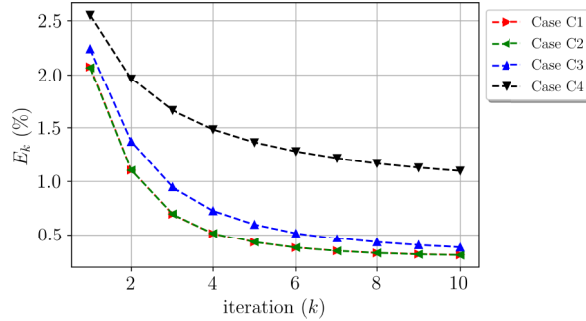


Figure 7: Simple phantom Case C. Relative L^2 -error vs iteration number. The initial error ($k=0$) was 50%.

The simulation results for the simple phantom manifest that at least two components of two non-parallel interior measurements are required to have a very good reconstruction (Case B3). In previous studies [13, 12, 6, 11, 14], it was shown that knowledge of at least two non-parallel interior \mathbf{J} or $|\mathbf{J}|$ are vital to reconstruct conductivity. In this study for the first time, we have demonstrated that knowledge of two non-parallel interior \mathbf{J} are sufficient for reconstruction. Figure 8 shows the result for this case in 3D representation sliced at 6 mm along each axis. As seen, a sharp reconstruction is obtained in each direction and the result is quite satisfactory.

Moreover, the simple phantom simulations show that increasing the number of interior measurements cannot compensate for the lack of enough components of \mathbf{J} . In addition, if one is interested in only one slices of the conductivity in a certain direction, only one component of one interior measurement with proper choice of boundary condition can produce satisfactory result.

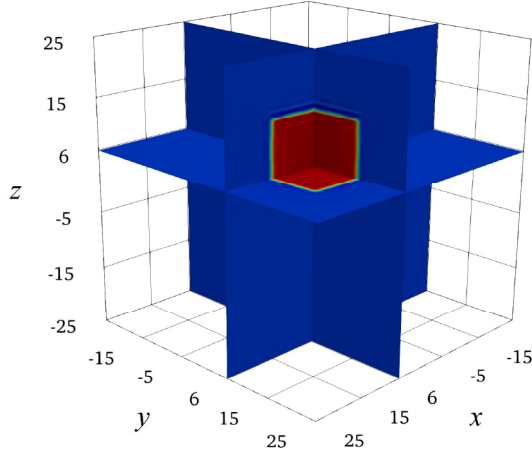


Figure 8: Simple phantom. A 3D representation for Case B3 sliced at 6 mm along each axis. This case shows the result for the minimum ICDI to obtain a good reconstruction.

4.2. Complex phantom

In this subsection the results for the complex phantom is presented. Based on the results from the previous section, we only simulate Case B for the complex phantom in which two interior measurements are considered.

The first row of Figure 9 shows three slices of the true conductivity distribution for the central (a) the x -axis slice, (b) the y -axis slice, and (c) the z -axis slice. The second to the fifth rows correspond to Case B1, Case B2, Case B3, and Case B4, respectively. The number of iterations was $K = 25$. The elapsed time and required memory were less than 30 minutes and 77 GB, respectively. The size of finite element matrix was about $(4.6 \cdot 10^7) \times (4.6 \cdot 10^7)$.

As can be seen from Figure 9, good results are found for Case B1 and Case B3 in all slices. However, for Case B2 and Case B4 severe artifacts appear. It is noteworthy that the results for Case B2 are in contrast to those obtained for the simple phantom. It may be related to the complex nature of the data used in this case, (2b), and the complexity of the phantom.

Figure 10 shows the relative L^2 -error of the reconstructed conductivity image at each iteration for the various cases. The initial error ($k = 0$) was 50%. This indicates that several iterations are required to reach a satisfactory level in contrast to the results for the simple phantom. The error patterns almost show an exponentially convergence for Case B1, B3, and B4. However, for Case B2 after iteration 4, the error starts to fluctuate. In this case the algorithm converges to a wrong value as shown by the third row of Figure 9.

It is worthwhile mentioning that a part of the error shown in Figure 10 is a result of the interpolation of the data to the reconstruction mesh. As mentioned before, to avoid committing an inverse crime, different meshes have been used for generating data and reconstruction.

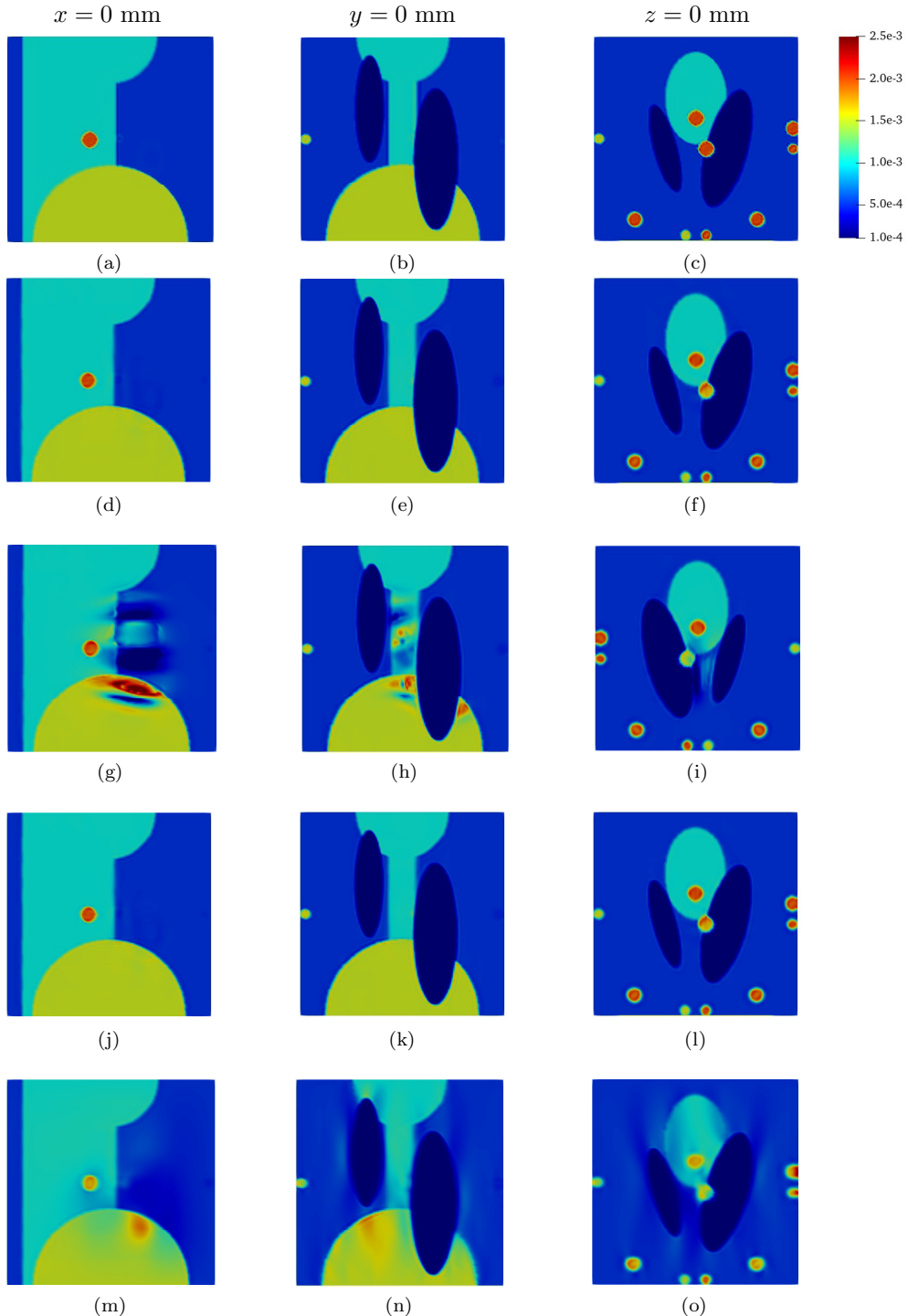


Figure 9: Complex Phantom Case B. The first to the third columns correspond to central the x -axis slice, the y -axis slice, and the z -axis slice, respectively. The first row is the true conductivity distribution. The second to the fifth rows correspond to Case B1, Case B2, Case B3, and Case B4, respectively. The number of iterations was $K = 25$.

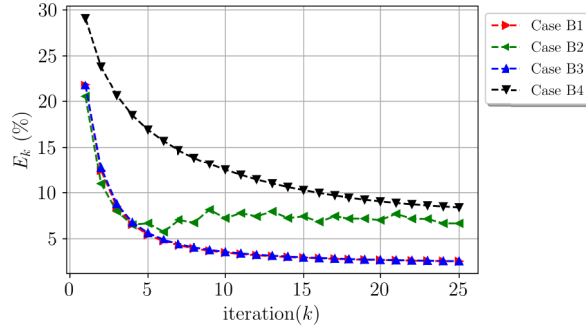


Figure 10: Complex phantom Case B. Relative L^2 -error vs iteration number. The initial error ($k=0$) was 50%.

For Case B2, we experimented with the regularized version of the algorithm (Eq. (19)). The regularization parameter α was optimally set to 2×10^{-1} which was found by trial and error. Figure 11 shows the reconstruction. Compared to the unregularized case (third row in Figure 9), the result improves significantly. Figure 12 compares the relative error for the regularized and unregularized cases during the iteration. Clearly, the use of regularization is attractive. For Case B4, we also tried the regularized version of the algorithm (Eq. (19)) with various α without improving the results.

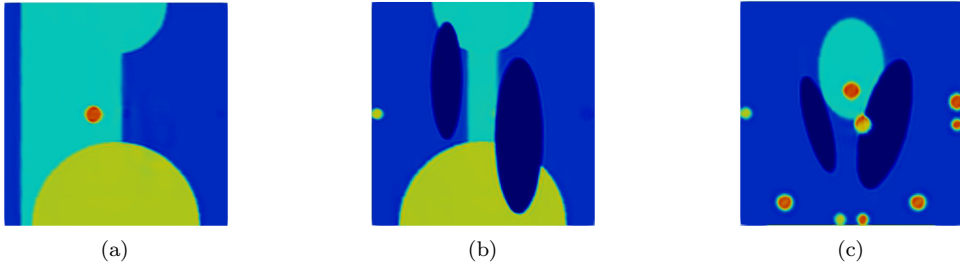


Figure 11: Complex Phantom Case B2. (a) Central x -axis, (b) Central y -axis, and (c) Central z -axis slice. The regularized reconstruction algorithm with $\alpha = 2 \times 10^{-1}$ has been used. The number of iterations was $K = 25$.

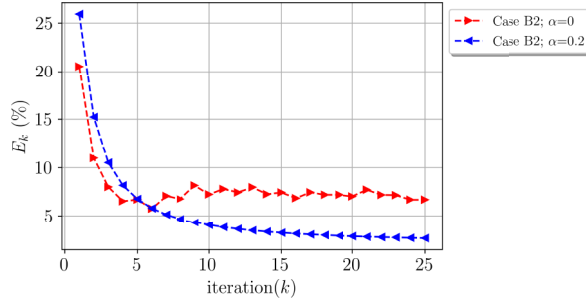


Figure 12: Complex phantom Case B2. Comparison of relative L^2 -error for unregularized (red dashed line with right triangle) and regularized (blue dashed line with left triangle) cases. The initial error ($k=0$) was 50%.

Similar to the simple phantom, the simulation results for the complex phantom manifest that at least two components of two non-parallel interior measurements (Case B3) are required to have a very good reconstruction. Figure 13 shows the result for this case in 3D representation sliced along the z -axis. As seen, the result is quite satisfactory.

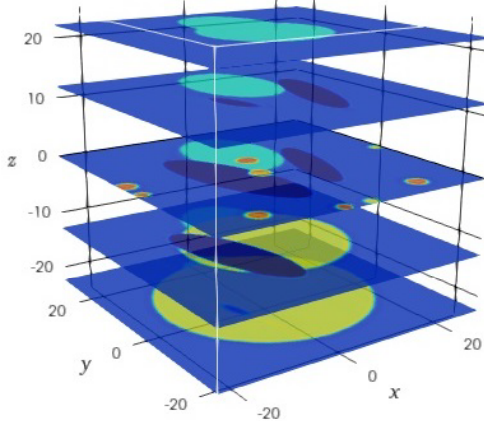


Figure 13: Complex phantom. A 3D representation for Case B3 sliced along z -axis. This case shows the result for the minimum ICDI to obtain a good reconstruction.

4.3. Noise Analysis

From the previous sections, we see that reasonable reconstructions can be obtained in the case of noise-free data with at least two components of two non-parallel interior measurements (Case B3). In this section, we consider the same problem, now with noisy data. Noise samples were i.i.d Gaussian random variable with mean 0 and variance 1. These samples were fed to (21) and different relative noise levels of $\delta = 20\%$, 40% , and 80% were considered.

Figure 14 shows the relative L^2 -error of the reconstructed conductivity at each iteration for the complex phantom Case B3 with various relative noise levels. Black dashed line with left triangle, blue dashed line with right triangle, and red dashed

line with down triangle correspond to $\delta = 0.2, 0.4$, and 0.8 , respectively. Comparing Figure 14 with Case B3 in Figure 10 at $k = 25$ shows that the noise increases the reconstruction error about 1%, 3%, and 7% for $\delta = 0.2, 0.4$, and 0.8 , respectively. Figure 14 illustrates that the algorithm exhibits so-called semi-convergence for $\delta = 0.4$ and 0.8 . We also performed this experiment for 16 realizations of the noise and then calculated the average of the error for each iteration. The obtained result was very close to that of obtained from a single noise realization.

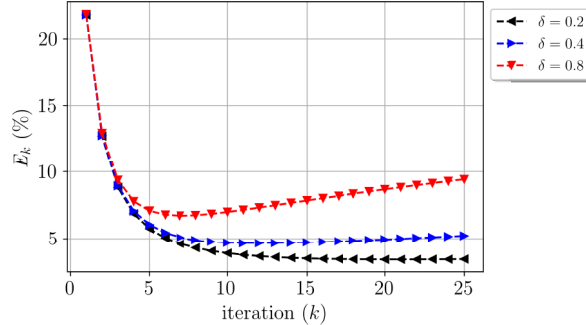


Figure 14: Complex phantom Case B3, Noise study. Relative error vs iteration number for various δ . The initial error ($k=0$) was 50%.

Figure 15 shows the results of reconstruction for noisy data with 80% relative noise level in Case B3 at $k=7$. Comparing the figure to Figure 9 shows that one can obtain a good reconstruction from highly noisy data by at least having two components of two non-parallel interior current density information. As can be seen, internal objects are distinguished fairly well in the figure. Redundancy in data can be a reason for this observation. We also tested the noisy data for Case C3. However, increasing the number of interior measurements did not improve the result significantly.

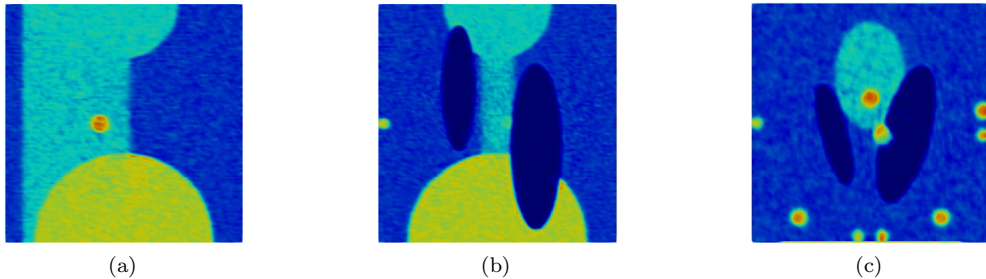


Figure 15: Complex phantom Case B3, Noise study ($\delta = 0.8$). (a) Central x -axis, (b) Central y -axis, and (c) Central z -axis slice. The results were shown for $k = 7$.

As shown by Figure 16, for noisy data, we tested the regularized version of the algorithm (Eq. (19)) for $\alpha = 0.1, 1$, and 2 . It seems that the best one is $\alpha = 1$, however the relative error for this case at $k = 25$ is equal to that of for unregularized algorithm ($\alpha=0$) at $k = 7$. Consequently, the regularization did not improve the result of reconstruction.

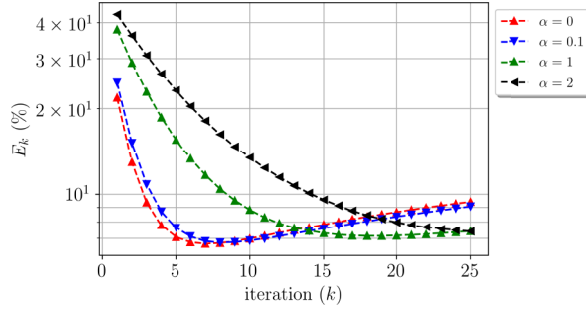


Figure 16: Complex phantom Case B3, Study of various regularization parameter α for noisy data ($\delta = 0.8$). Relative error vs iteration number. The initial error ($k=0$) was 50%.

4.4. Benchmarking against the J -substitution method

Our computational study above shows that from two components of two non-parallel interior current densities, good reconstructions can be obtained. In this section, we benchmark the result to the well-known J -substitution method [15]. Inspired by [20], we adapt the method to reconstruct the conductivity from full \mathbf{J} data and M interior measurements in iteration k as follows:

$$\sigma^{k+1} = -\frac{\sum_{m=1}^M \langle \mathbf{J}_m, \nabla u_m^k \rangle}{\sum_{m=1}^M \langle \nabla u_m^k, \nabla u_m^k \rangle} \quad (22)$$

where $\langle \cdot, \cdot \rangle$ denotes the $L^2(\Omega)$ inner product. When data is in the form (2c) and (2d), the missing components of \mathbf{J} are obtained iteratively by solving the forward problem with conductivity σ^k . We evaluate the J -substitution method using the complex phantom.

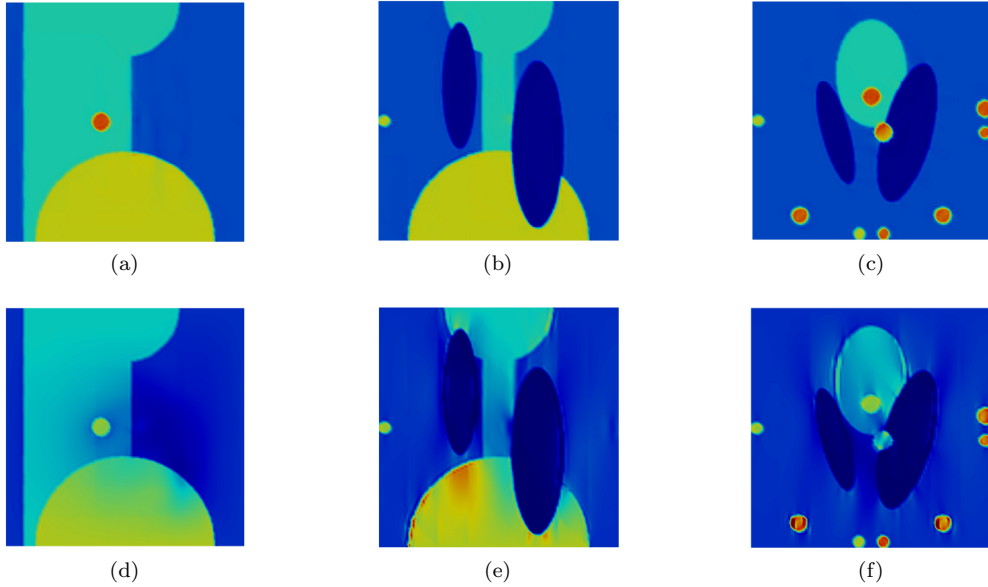


Figure 17: Complex phantom, J -substitution method. The first to the third columns correspond to central the x -axis slice, the y -axis slice, and the z -axis slice, respectively. The first and the second rows correspond to Case B3 and Case B4, respectively. The number of iterations was $K = 25$.

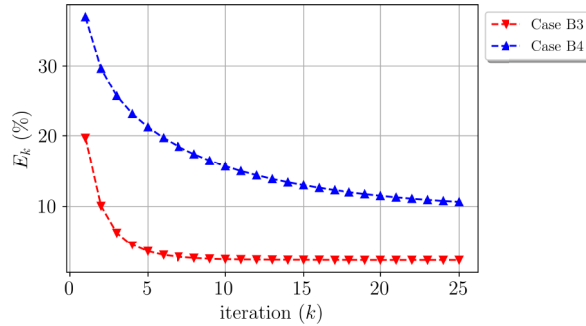


Figure 18: Complex phantom, J -substitution method. Relative error vs iteration number for Case B3 and Case B4. The initial error ($k=0$) was 50%.

Figure 17 shows the results of reconstruction for the J -substitution method. The first and the second rows correspond to Case B3 and Case B4, respectively. The number of iterations was $K = 25$. The elapsed time and the required memory were less than 6 minutes and 16 GB, respectively.

As seen from Figure 17 very good reconstructions are found for Case B3 whereas severe artifacts appear for Case B4. Results support the outcome of previous simulations. Figure 18 shows the relative L^2 -error of the reconstructed conductivity image at each iteration for Case B3 and Case B4. The initial error ($k = 0$) was 50%. In

Table 4: Percentage of relative error of J -substitution method and Newton algorithm for noisy data with different δ values. The number of iterations was $K = 5$.

Relative noise level (δ)	Relative error (%)	
	J -substitution method	Newton algorithm
0	4%	5%
0.5	8%	6%
1	14%	8%
2	27%	11%
4	49%	18%

terms of convergence, it is almost similar to results obtained for the Newton algorithm (Figure 10). The error patterns show an exponentially convergence.

We now compare the performance of the J -substitution method and the Newton algorithm for Case B3 on noisy data with different δ values. Table 4 shows the percentage of relative error for each method. The complex phantom was used and the number of iterations was set to $K = 5$. The elapsed time was less than 3 minutes and 7 minutes for the J -substitution method and the Newton algorithm, respectively. The required memory was less than 16 GB and 80 GB for the J -substitution method and the Newton algorithm, respectively.

As seen from Table 4, the Newton algorithm is more robust against the noise in comparison with the J -substitution method. However, the Newton method achieves this at the cost of much more computational expenses. Figure 19 shows the reconstructed conductivity images for Case B3 and $\delta = 2$. The first to the third columns correspond to central the x -axis slice, the y -axis slice, and the z -axis slice, respectively. The first and the second rows corresponds to the the Newton algorithm and J -substitution method, respectively. As can be seen, the Newton algorithm has a superior performance over the J -substitution method.

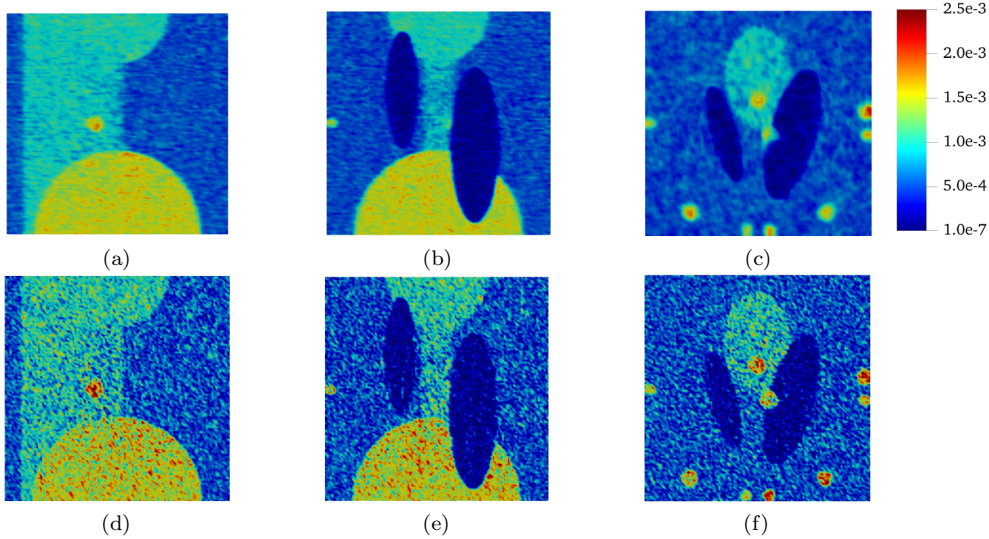


Figure 19: Complex phantom Case B3, Newton algorithm vs J -substitution method for noisy data with $\delta = 2$. The first to the third columns correspond to central the x -axis slice, the y -axis slice, and the z -axis slice, respectively. The first and the second rows corresponds to the the Newton algorithm and J -substitution method, respectively. The number of iterations was $K = 5$.

5. Conclusion

In this paper, we studied the conductivity image reconstruction in three dimensions using full and partial interior current density information. The main findings can be summarized as follows:

- Conductivity reconstruction by ICDI has the potential for high resolution and high contrast reconstruction of the electrical conductivity in a conducting medium.
- The reconstructions are excellent when two components of the interior current density are available for two non-parallel fields. Results from both the the Newton algorithm and J -substitution method confirm this outcome. We conjecture that a rigorous proof of this observation can eventuaaly be found; this is work in progress. It is very important result for imaging technologies that use only one component of \mathbf{B} , B_z , to reconstruct the conductivity, since B_z only contains information about the two components J_x, J_y of \mathbf{J} .
- Increasing the number of interior measurements corresponding to different boundary conditions cannot compensate for the lack of components in \mathbf{J} .
- If one is interested in only one slices of the conductivity in a certain direction, only one component of one interior measurement with the proper choice of boundary condition can produce satisfactory result.
- Conductivity reconstruction from ICDI by the Newton algorithm is highly robust against noise in the data. Even when the relative noise more than 80%, reasonable reconstructions are obtained. On the other hand, reconstructions by the J -substitution method has a low computational costs.

The results hold promise for the near real-time and high resolution conductivity reconstruction in the practical applications where only one component of the magnetic field B_z is available. For the future studies, we aim to develop the algorithm to reconstruct σ directly from B_z and then embed a fast forward solver of MREIT like [34] to the algorithm. Moreover, further studies can be done for considering anisotropic conductivity distribution, realistic human head phantom, and experimental data for reconstruction. The conclusions from this study can most likely be extended to other reconstruction methods for CDII as well.

Acknowledgement

This study was supported by the Danish Council for Independent Research | Natural Sciences (grant number 4002-00123). The work was initiated while Hassan Yazdanian was a visiting PhD student at the Department of Applied Mathematics and Computer Sciences, Technical University of Denmark.

References

- [1] Zou Y, Guo Z. A review of electrical impedance techniques for breast cancer detection. *Medical Engineering & Physics*. 2003;25(2):79–90.
- [2] Michel CM, Murray MM, Lantz G, Gonzalez S, Spinelli L, de Peralta RG. EEG source imaging. *Clinical Neurophysiology*. 2004;115(10):2195–2222.
- [3] Schmidt C, Wagner S, Burger M, Rienen Uv, Wolters CH. Impact of uncertain head tissue conductivity in the optimization of transcranial direct current stimulation for an auditory target. *Journal of Neural Engineering*. 2015;12(4):046028.
- [4] Widlak T, Scherzer O. Hybrid tomography for conductivity imaging. *Inverse Problems*. 2012;28(8):084008.
- [5] Seo JK, Woo EJ. Magnetic resonance electrical impedance tomography (MREIT). *SIAM Review*. 2011;53(1):40–68.
- [6] Hasanov KF, Ma AW, Nachman AI, Joy ML. Current density impedance imaging. *IEEE Transactions on Medical Imaging*. 2008;27(9):1301–1309.
- [7] Nachman A, Tamasan A, Timonov A. Recovering the conductivity from a single measurement of interior data. *Inverse Problems*. 2009;25(3):035014.
- [8] Ider YZ, Birgül Ö. Use of the magnetic field generated by the internal distribution of injected currents for electrical impedance tomography (MR-EIT). *Turkish Journal of Electrical Engineering & Computer Sciences*. 2000;6(3):215–226.
- [9] Kwon O, Lee JY, Yoon JR. Equipotential line method for magnetic resonance electrical impedance tomography. *Inverse Problems*. 2002;18(4):1089.
- [10] Özdemir MS, Eyüboğlu BM, Oezbek O. Equipotential projection-based magnetic resonance electrical impedance tomography and experimental realization. *Physics in Medicine & Biology*. 2004;49(20):4765.
- [11] Ider YZ, Onart S, Lionheart WR. Uniqueness and reconstruction in magnetic resonance-electrical impedance tomography (MR-EIT). *Physiological Measurement*. 2003;24(2):591.
- [12] Joy M, Nachman A, Hasanov K, Yoon R, Ma A. A new approach to current density impedance imaging (CDII). In: Proc. International Society for Magnetic Resonance in Medicine. vol. 356. Kyoto, Japan; 2004. p. 2356.
- [13] Lee JY. A reconstruction formula and uniqueness of conductivity in MREIT using two internal current distributions. *Inverse Problems*. 2004;20(3):847.
- [14] Elsaïd NM, Nachman AI, Ma W, DeMonte TP, Joy ML. The impact of anisotropy on the accuracy of conductivity imaging: A quantitative validation study. *IEEE Transactions on Medical Imaging*. 2016;36(2):507–517.
- [15] Kwon O, Woo EJ, Yoon JR, Seo JK. Magnetic resonance electrical impedance tomography (MREIT): simulation study of J-substitution algorithm. *IEEE Transactions on Biomedical Engineering*. 2002;49(2):160–167.
- [16] Kim YJ, Kwon O, Seo JK, Woo EJ. Uniqueness and convergence of conductivity image reconstruction in magnetic resonance electrical impedance tomography. *Inverse Problems*. 2003;19(5):1213.

- [17] Kim S, Kwon O, Seo JK, Yoon JR. On a nonlinear partial differential equation arising in magnetic resonance electrical impedance tomography. *SIAM Journal on Mathematical Analysis*. 2002;34(3):511–526.
- [18] Nam HS, Lee BI, Choi J, Park C, Kwon OI. Conductivity imaging with low level current injection using transversal J-substitution algorithm in MREIT. *Physics in Medicine & Biology*. 2007;52(22):6717.
- [19] Liu Y, Zhu S, He B. Induced current magnetic resonance electrical impedance tomography of brain tissues based on the J-substitution algorithm: a simulation study. *Physics in Medicine & Biology*. 2009;54(14):4561.
- [20] Sajib SZ, Katouch N, Kim HJ, Kwon OI, Woo EJ. Software toolbox for low-frequency conductivity and current density imaging using MRI. *IEEE Transactions on Biomedical Engineering*. 2017;64(11):2505–2514.
- [21] Park C, Lee BI, Kwon OI. Analysis of recoverable current from one component of magnetic flux density in MREIT and MRCDI. *Physics in Medicine & Biology*. 2007;52(11):3001.
- [22] Nachman A, Tamasan A, Timonov A. Current density impedance imaging. In: Guillaume B, et al., editors. *Tomography and Inverse Transport Theory*. vol. 559 of *Contemporary Mathematics*. AMS; 2011. p. 135–149.
- [23] Nachman A, Tamasan A, Timonov A. Reconstruction of planar conductivities in subdomains from incomplete data. *SIAM Journal on Applied Mathematics*. 2010;70(8):3342–3362.
- [24] Montaldo C, Stefanov P. Stability of coupled-physics inverse problems with one internal measurement. *Inverse Problems*. 2013;29(12):125004.
- [25] Alberti GS, Capdeboscq Y, Capdeboscq Y. Lectures on elliptic methods for hybrid inverse problems. vol. 25. Société Mathématique de France Paris; 2018.
- [26] Bal G. Hybrid inverse problems and internal functionals. In: *Inverse problems and applications: inside out. II*. vol. 60 of *Math. Sci. Res. Inst. Publ.* Cambridge Univ. Press, Cambridge; 2013. p. 325–368.
- [27] Hoffmann K, Knudsen K. Iterative reconstruction methods for hybrid inverse problems in impedance tomography. *Sensing and Imaging*. 2014;15(1):96.
- [28] Bal G, Hoffmann K, Knudsen K. Propagation of singularities for linearised hybrid data impedance tomography. *Inverse Problems*. 2017;34(2):024001.
- [29] Logg A, Mardal KA, Wells G. Automated solution of differential equations by the finite element method: The FEniCS book. vol. 84. Springer-Verlag Berlin Heidelberg; 2012.
- [30] Ayachit U. The ParaView guide: a parallel visualization application. Clifton Park, USA: Kitware; 2015.
- [31] Bochev PB, Gunzburger MD. Least-squares finite element methods. vol. 166. Springer; 2009.
- [32] Kwon O, Park C, Park EJ, Seo JK, Woo EJ. Electrical conductivity imaging using a variational method in Bz-based MREIT. *Inverse Problems*. 2005;21(3):969.
- [33] Shepp LA, Logan BF. The Fourier reconstruction of a head section. *IEEE Transactions on Nuclear Science*. 1974;21(3):21–43.
- [34] Yazdanian H, Saturnino GB, Thielscher A, Knudsen K. Fast evaluation of the Biot-Savart integral using FFT for electrical conductivity imaging. *Journal of Computational Physics*. 2020;411:109408.